RSC Advances

ROYAL SOCIETY OF CHEMISTRY

www.rsc.org/advances

RSC Advances

ARTICLE

Development of multifunctional TiO_2/MWCNT hybrid composite grafted on stainless-steel grating

Received 00th January 20xx,
Accepted 00th January 20xx

DOI: 10.1039/x0xx00000x

www.rsc.org/

Sara Cravanzola,[a] Sagar M. Jain,[a,b] Federico Cesano,[a]* Alessandro Damin,[a] and Domenica Scarano[a]

Functional materials have promising potentialities to fabricate new devices with improved properties, to meet many requirements, including environmental issues. Along these themes, a multiphase structure made by TiO_2/MWCNTs hybrid nanoscaffold grafted on a metal grating (stainless-steel type), acting as a strong, highly durable and heat/thermal inert support, is proposed. The method, consisting in the fabrication of a porous scaffold, via catalytic-CVD of MWCNT forest on the stainless-steel first, followed by the grafting of nanocrystalline TiO_2 via sol-gel method and then calcination, is simple and effective. Morphology, structure and optical properties have been investigated by means of XRD, SEM, AFM, HRTEM microscopies, Raman and UV-visible spectroscopies, and porosity analysis. Interestingly, the TiO_2/MWCNTs hybrid composite exhibits enhanced photocatalytic activity as compared to the TiO_2, obtained by adopting the same preparation. More interestingly, the hybrid system exhibits additional functionalities, such as magnetic, surface and optical properties. The multifunctional approach allows to combine the enhancement of the photodegradation with magnetic properties, which can make the recovery of the solution from the photocatalyst more easy. Furthermore, it will be shown that, by moving from MWCNT/stainless-steel to TiO_2/MWCNT/stainless-steel composites, the surface character changes from hydrophobic to hydrophilic in nature. The grafting on the stainless-steel support allows a broad range of application fields, including combined strength and corrosion resistance in aqueous solutions at ambient temperature, together with enhancement of electrical, optical and photocatalytic properties.

1. Introduction

Hybrid nanomaterials are of particular interest because of their improved properties and promising technological applications, including sensors and biosensors, electrical and optical devices, solar cells, catalysis and photocatalysis.[1-7] As a matter of fact, the combined employment of different nanostructures and nanophases to form hybrid and/or composite architectures, may allow to fabricate multifunctional materials, in which each constituent brings one or more properties, such as structural (i.e. strength, durability, mechanical properties) and non-structural functions (i.e. electrical and thermal conductivity, sensing, energy harvesting/storage properties). According to this, layered materials incorporated into polymers (metal-organic frameworks nanosheets) or consisting of intercalated ferromagnetic layers (CoAl-based layered-double-hydroxides) allows outstanding CO_2 separation from CO_2/CH_4 gas mixtures or thermoresponsive switching ability, respectively.[8, 9] As far as photocatalysis is concerned, an enhanced photocatalytic performance in the photodegradation of methylene blue (MB) has been obtained by the amorphous TiO_2/ZnO hybrid nanorods, as compared to pure components.[10]

Among the many constituents of the hybrid composites, TiO_2 and carbon nanotubes (CNTs) have attracted considerable attention because of their outstanding optical, photoelectrochemical and electronic properties.[11] Mixed-phase TiO_2-based composites show higher photoreactivity in comparison with pure materials, due to the formation of solid-solid interfaces that can improve: i) charge transfer and spatial separation, ii) reduced electron-hole recombination and interface defective sites that act as catalytic "hot spots".[12-16]

In fact, the incorporation of CNTs into the TiO_2 matrix can enhance the conductivity of the TiO_2 aggregates and facilitate a faster electron transport across the TiO_2 network, thus minimizing charge recombination and ensuring a high photoactivity. Moreover, the synergy effect of activated carbon and TiO_2 has been shown for the photocatalytic degradation of organic compounds.[17]

These are crucial points, as recently TiO_2 has been mainly used in the decomposition of toxic and hazardous organic pollutants in contaminated water and air, which are of great importance for both health and environmental protection.[18-23]

However, the high photocatalytic activity of TiO_2 nanoparticles is not the sole requisite for practical applications because, for photocatalysis processes in liquid media, the separation of TiO_2 material from the water solution after irradiation is mandatory.[24]

[a] Department of Chemistry, NIS (Nanostructured Interfaces and Surfaces) Interdepartmental Centre and INSTM Centro Di Riferimento, University of Torino, Via P. Giuria, 7, 10125 Torino, Italy. * E-mail: federico.cesano@unito.it
[b] Current Address: sagarmjain@gmail.com.

†Electronic Supplementary Information (ESI) available: Additional figures and material characterization (SEM/EDAX, N_2-adsorption/desorption isotherms, hydrophilic/phobic surface properties. See DOI: 10.1039/x0xx00000x

TiO_2 microaggregates (instead of very small and isolated particles) are preferred in this regard, because they make more effective the separation of the photocatalyst from the reaction medium.[25] Following many authors, several approaches to control the size/shape, porosity, agglomeration and nature of TiO_2 nanoparticles and films have been adopted.[26-36] Among all investigated methods, template-based procedures look ideal for controlling and adapting the TiO_2 texture because the pore sizes of the templating scaffold, where the material is under formation, can be accurately tailored.[37, 38] In this regard, it has been observed that the surface roughness and composition, the thermal and the chemical stability of the substrate have a direct influence on the purity, crystallinity, mesostructural ordering and on the photocatalytic activity of the obtained TiO_2 films.[39] Industrially important support materials like stainless steel alloys have been investigated by few groups.[39-43]

Following this line, in this work a TiO_2/MWCNT/stainless steel AISI 304 grating composite is prepared by chemical vapor deposition of MWCNTs and by a sol-gel synthesis of TiO_2. Although the growth of MWCNTs on stainless-steel support, promoted by internal (via chemical etching) or external catalysts is not new,[44-49] it will be shown that the formation of hybrid TiO_2/MWCNT scaffold on stainless steel exhibits unprecedented multifunctional properties.

The role of each component within the composite can be summarized, as follows: i) TiO_2 is the working photocatalyst; ii) the multiwalled carbon nanotube (MWCNT) forest is acting as a nanostructured support and as a templating phase, iii) the stainless steel expanded metal grating acts as a heat/chemical resistant, durable and strong scaffold. Moreover, it will be shown that, besides the above-mentioned properties, the porosity of the hybrid structures, as well as the inter-phase contacts, the surface character and magnetic properties can be suitably exploited to design multifunctional materials.

The composite grating has been characterized by means of scanning electrical microscopy (SEM), atomic force microscopy (AFM), Raman spectroscopy, transmission electron microscopy (TEM), X-ray diffraction (XRD), energy dispersive spectroscopy (EDS) and thermogravimetric analysis (TGA). The catalytic activity of the TiO_2/MWCNTs/stainless-steel composite grating has been investigated by means of UV-vis spectroscopy, following the degradation of methylene-blue (MB) under solar irradiation.

2. Experimental

2.1 Materials

Synthesis of MWCNTs on the stainless steel expanded grating. Aligned MWCNTs, often called as "MWCNT forest", were obtained by means of the catalytic chemical vapor deposition (CCVD) process in a horizontal tube reactor (d_{tube}=2.5 cm) by using ferrocene as a catalyst, on a two 304 stainless-steel gratings used as substrates (having high temperature oxidation resistance) (Fig. S1, ESI†). The supports were placed in the middle of the quartz tube first and the temperature of the oven was increased up to 800°C (heating rate: 20°C/min) under N_2 gas flow (70 ml/min). Then a C_2H_4/H_2 gas mixture (100ml + 25 ml) was introduced (total flow 90 ml/min) for 1h, then the gas flow was switched to N_2 and the temperature reduced.

Synthesis of TiO_2 on the MWCNTs Steel Composite. A TiO_2 sol-gel solution was first prepared by starting from 7.04 mmol of Ti isopropoxide (TIP) in 25.4 ml of isopropyl alcohol (IPA) and concentrated HNO_3 (20 mmol) with the addition of 0.4 ml of distilled water at about 50°C under magnetic stirring. Then, the MWCNTs/stainless steel gratings were dipped in the solution for 1h at RT under stirring, dried at 80°C and calcined at 400°C in air for 1h. Although a higher temperature would increase the crystallinity/photoactivity of TiO_2 nanocrystals, the thermal treatment in air has been set to 400°C to obtain nearly crystalline anatase nanoparticles, thus preventing the extensive oxidation of MWCNTs. As a matter of fact, it is known that from the thermogravimetric (TG) profile of the carbon nanotubes coming from the second sample grid, beside the phases quantify of the hybrid material (vide infra), the products coming after complete oxidation are obtained.

2.2 Methods

The structure and the morphology of the as grown CNTs were investigated by Raman spectroscopy, by scanning electron microscopy (SEM) and by atomic force microscopy (AFM), while the TiO_2/MWCNTs hybrid system was investigated by scanning and transmission electron microscopies. The Raman spectra were acquired by using a micro–Raman Renishaw spectrometer equipped with a CCD detector. The 514 nm (green) and 785 nm (red) laser lines were used to excite the samples. All the measurements were performed at room temperature: the reference samples were analysed in powder form, whereas the as grown CNTs were directly investigated on the support metal grating. The SEM images were taken on a Zeiss Evo 50 SEM instrument operating at 30 kV; the AFM images with a Park Systems XE-100 in non-contact mode; the TEM images with a JEOL 3010-UHR instrument operating at 300 kV, equipped with a 2k×2k pixel Gatan US1000CCD camera.

The photodegradation experiments of methylene blue (MB) have been followed by means of the UV-vis spectroscopy (Varian Cary UV 5000) on the TiO_2/MWCNTs hybrid system grafted to the metal grating, on the as-prepared TiO_2 and on TiO_2 (P25) centrifuged solutions (used as a reference system). The gradual disappearance of the bands of MB adsorbed on the different systems upon exposure to visible light for increasing time was investigated. Photoluminescence (PL) spectra have been obtained at RT by using an excitation incident light of 325 nm, coming from a conventional Xe arc lamp (HORIBA Jobin Yvon Fluorolog-3 instrument). To minimize reflections of the incident light, samples have been placed at 15° from the specular direction.

X-ray diffraction patterns on samples have been collected with a diffractometer (PANalytical PW3050/60 X'Pert PROMPD) by using a Ni-filtered Cu anode and working with reflectance Bragg–Brentano geometry. Qualitative phase identification from the XRD data is based on the International Center for Diffraction Data (ICDD) powder diffraction files.

Weight ratios of TiO_2 and of MWCNTs have been obtained from the TG curve profile of TiO_2/MWCNT hybrid material, scratched away from the second steel substrate, which has been also thermally

treated up to 800°C in N_2 gas flow first. Then, during the subsequent isothermal treatment (800°C) the gas flow has been switched to air. The observed residual weight (≈25%wt) and weight loss (≈75%wt) are associated with the TiO_2 amount and with the MWCNT quantity after complete oxidation, respectively (Fig. S6, ESI†). In a second experiment, total weight of MWCNTs on the steel grids, and hence the total amount of the TiO_2 phase, has been obtained from the weight analysis of the second sample before and after the thermal oxidation (800°C).

N_2 adsorption–desorption experiments have been carried out at 77 K (Micromeritics ASAP 2020 instrument) to determine the Brunauer–Emmett–Teller (BET) surface area and the micropore volume (t-plot method). A powder sample was gently scratched from the TiO_2/MWCNTs composite, while the TiO_2 sample was investigated as obtained. The surface area of the samples was determined after outgassing at 150°C overnight. The pore size distributions (PSDs) were obtained by means of a non-negative least squares fitting of the absorption isotherm data by applying the Density Functional Theory (DFT) method (NLDFT model, cylinder as a geometry) with ASAP 2020 4.0 software (Micromeritics). Microporous (S_{micro}) and mesoporous (S_{meso}) surfaces were obtained from t-plot method (*Harkins and Jura* thickness curve) and from $S_{meso} = S_{tot} - S_{micro}$, respectively.

Photodegradation test. The TiO_2/MWCNTs hybrid system grafted to the metal grating and the powder samples (5.1 mg TiO_2 coming from the sol-gel preparation, together with 5.1 mg P25 TiO_2) were dispersed in 8.5 ml of methylene blue (MB) water solution (12.5 mg/L). Then the samples were kept under the dark at RT for 1 hour. Before exposing to the solar lamp, MB-as prepared TiO_2 and MB-P25 TiO_2 dispersions were centrifuged at 10000 rpm for 20 min.

Photocatalytic degradation of the MB has been investigated by UV-vis spectroscopy. The light solar simulating irradiation was carried out at 25°C±5 by means of a SOL2/500S lamp (Honle UV technology, Munchen, Germany). The SOL-bulb and the H_2 filter together yield a spectrum, which is very similar to the natural sunlight, ranging from ultraviolet to infrared radiation (~295-3000 nm). The integrated intensity of the adsorbed MB manifestations (C) was used to obtain the C/C_0 *vs*. time plots, where C_0 is the concentration, corresponding to the initial intensity before illumination. A comparative photodegradation test of the TiO_2/MWCNT/grating system and of the P25 reference TiO_2 powder has also been performed for several cycles (six cycles). After each cycle, samples have been magnetically extracted and dried (TiO_2/MWCNT/grating system) or obtained after filtering and drying the nanopowder (P25).

3. Results and Discussion

3.1 Morphology and Structure of TiO_2/MWCNTs Grafted on the Stainless-Steel

The structure and the composition of the TiO_2/MWCNT hybrid nanostructures on the stainless steel expanded metal grating are schematized in Scheme 1.

The multiphase system was obtained by starting from a stainless steel support (Scheme 1a) (see SEM and EDAX analyses of steel support in Fig. S1, ESI†), which first was used as a substrate to grow densely packed MWCNTs (Scheme 1b, Step 1). Then, MWCNTs-covered stainless-steel grating was dipped in a sol-gel solution containing the TiO_2 precursor and calcinated at 400°C to obtain the final TiO_2/MWCNTs/steel multiphase structure (Scheme 1c, step 2).

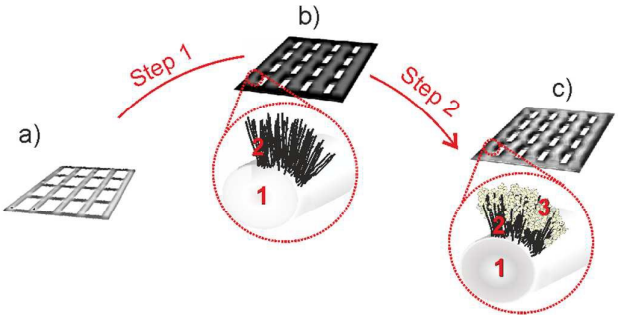

Scheme 1. Preparation steps to fabricate the hybrid TiO_2/MWCNTs/steel structure: Step 1 – synthesis of MWCNTs on the stainless steel grating. Step 2 – grafting of nanocrystalline TiO_2 nanoparticles on the MWCNTs support via sol-gel method and calcination at 400°C. The multiphase structure is also schematized: 1-stainless steel grating; 2-MWCNT forest and 3-nanocrystalline porous TiO_2 layer.

XRD diffraction measurements have been performed to follow the preparation steps as described in Scheme 1 (Fig. 1). In particular, Fig. 1 compares patterns of: a) the support; b) the MWCNT forest/stainless steel composite; c) the MWCNT forest/stainless stainless-steel composite after impregnation with a TIP sol-gel solution and after the thermal treatment at 400°C; d) the pure powder obtained by the same sol–gel method for MWCNTs/TiO_2 composites.

More in detail, moving from the a) pattern of the stainless steel (face-centred cubic phased Fe; γ-Fe) (PDF card #65-4150) to that of the MWCNTs/metal grating composite (pattern b), the complex envelope observed in the 2θ = 35-55° interval is best matched by cementite phase (Fe_3C, PDF card #35-0772) with the contribution of the small features at 2θ = 51° and 2θ = 74.6° due to the γ-Fe (austenitic stainless steel). Furthermore, the main peak around 2θ = 26.2° in the same pattern is due to the (002) crystalline planes of the graphite phase (PDF card #41-1487). On the basis of this figure, from the small FWHM (about 0.93°) of the (002) diffraction peak, a high graphitisation degree of the MWCNTs covering the grating can be singled out.

From the XRD feature located at 44.7°, which can be indexed with the (110) plane reflections of α-Fe (PDF #06-0696), and then confirmed from the Fe-C phase diagram, the contribution of the body-centred cubic phase α-Fe is inferred. The possible conversion of Fe during thermal treatments or the synthesis of CNTs is documented by some papers.[45, 50-52] In Fig. 1c and in the corresponding insert, the 2θ ≈ 24.6°-25.6° feature, due to the formation of TiO_2 phase, is also observed. From this, the simultaneous presence in the composite of the graphite and anatase (PDFcard #21-1272) phases can be highlighted, as compared with the pattern of the TiO_2 pure powder obtained from the sol-gel solution (Fig. 1d). Notice a further small contribution due to the weak and broad feature at 2θ = 30-33°, which can be indexed

with the (121) XRD reflection planes of Brookite (PDF card #29-1360) (Fig. 1d).

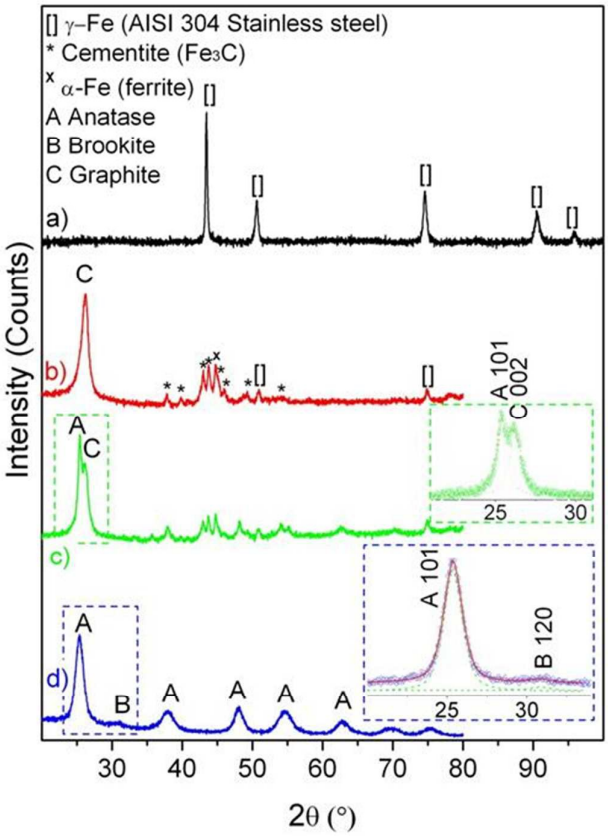

Fig. 1. XRD patterns of: a) the expanded metal grating used as a support; b) the MWCNTs/ metal grating composite; c) the MWCNTs/ metal grating composite after impregnation with a TIP sol-gel solution and thermal treatment at 400°C for 1h in air; d) the pure powder obtained from the sol-gel solution treated at the same temperature (400°C). XRD line positions of standards are reported for comparison: (A) anatase (PDF card #21-1272), (B) brookite (PDF card #29-1360), (C) graphite (PDF card #41-1487), (*) cementite (Fe_3C, PDF card #35-0772), ([]) γ-Fe (AISI 304 stainless steel) (fcc-phased Fe, PDF card #65-4150) and α-Fe (ferrite, bcc-phased Fe, PDF card # 06-0696) (X), respectively.

From the Scherrer's equation ($L = K\lambda/\beta \cos\vartheta$, where: λ is the X-ray wavelength, β is the FWHM of the diffraction line corrected by the instrumental broadening, ϑ is the diffraction angle, and K is a constant, which has been assumed to be 0.9), the mean crystallite size of the anatase particles was calculated. More in detail from the 2θ = 25.4° XRD peak (Fig. 1d), assigned to the (101) anatase crystalline planes, nanocrystals of about 6 nm in size are obtained.

3.2 Morphology and Structure of MWCNTs Grafted on Stainless-Steel-Metal Grating.

The carbon nanotube forest, obtained on the grating by means of the catalytic decomposition of C_2H_4 at 800°C for 1h is SEM and AFM imaged in Fig. 2. The low resolution top-view SEM images (Fig. 2a and the inset therein) illustrate that the carbon nanotubes are entirely covering the support, thus reducing the size of the cavities, which locally appear to be completely obstructed. From the high-resolution SEM image (Fig. 2b) densely packed carbon nanotubes with lengths, ranging in the 25-50 μm interval and protruding from the supporting grating, are shown. As no details are obtained at the nanometric scale on the emerging network of CNTs, more insights come from AFM analysis (Fig. 2c). From this, it comes that the emerging CNTs, about 20-30 nm in diameters, are vertically oriented. Besides, within the CNTs dense forest, pores about 20-60 nm in diameter can be highlighted, at the adopted resolution.

Raman spectroscopy provides an accurate investigation of the properties of the carbon-based materials, thus giving information on purity, structure, defectiveness and any presence of the amorphous carbon phase. All graphite-like materials, including MWCNTs, show a strong peak in the first-order Raman spectra, around 1580 cm^{-1} (G-band), which is the high-frequency E_{2g} first-order mode. Additional features in the first-order Raman spectra: D-band, around 1300-1350 cm^{-1}, and D'-band at about 1620 cm^{-1} are associated with more disordered phases (amorphous carbon) and exhibit dispersive behaviour, as these frequencies change as a function of the laser energy.[53-55] In particular, frequencies upshift linearly with increasing the excitation energy over a wide laser energy range. In the second-order region of the Raman spectra the main fingerprints in the 2650-2750 cm^{-1} interval (G'-band), are caused by two-phonon scattering around the K point of the Brillouin zone, which are again sensitive to increasing defect density.

Raman spectra obtained by means of λ=514 nm and λ=785 nm laser line excitations are shown in Fig. 2d. The green spectrum (λ=514 nm) evidences three distinct, well defined bands, with maxima at 1356 cm^{-1} (D-band), 1585 cm^{-1} (G-band) and 2708 cm^{-1} (G'-band), while the red spectrum (λ=785) shows a more complex situation.

As a matter of fact, on red spectrum, beside the two downward shifted bands at 1313 cm^{-1} (D-band) and 2624 cm^{-1} (G'-band), a more complex envelop with two maxima at 1586 cm^{-1} (G-band) and at 1612 cm^{-1} (D'-band) can be observed.

Although a detailed discussion of these spectra is beyond the scope of this paper and the reader can be referred elsewhere,[56] some fingerprints merit to be discussed. Beyond the general assignment, it is worthy noticing that in Raman spectrum obtained by 785 nm laser line excitation, the weak D'-band disorder-induced feature, which is silent under 514 nm illumination, is observed at 1612 cm^{-1}.

Notice that, in agreement with literature data, the G peak is quite independent of excitation wavelengths, conversely the D, D' and G' bands downshift with increasing wavelength and their relative intensity increases, being these phenomena explained by the double resonance theory.[57]

Moreover, as D' bands become as intense as the G-band for the excitation wavelengths in the infrared region, this has been considered distinctive of densely aligned and vertically oriented MWCNTs, which are grown perpendicular to the substrate,[58, 59] in agreement with our structural model. Some more, the observed small line-widths indicate that these features are representative of high quality MWCNTs with a very good structural order.[58]

In conclusion, we state that the synthesis of the MWCNTs forest on the stainless steel support with an external catalyst is more effective as compared to the same process without the external catalyst, as reported in the literature.[44-49]

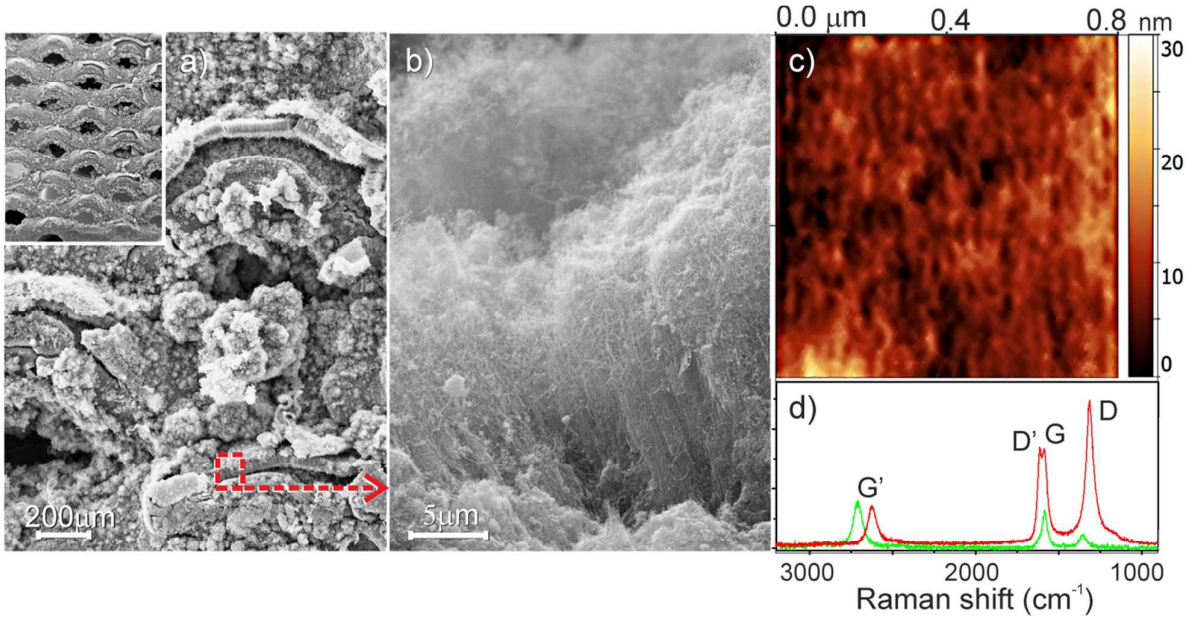

Fig. 2. a) Top-view SEM images of the stainless steel grating after the CNTs growth; b) enlarged view of a selected area on (a) SEM image; c) top-view 0.8x0.8μm nc-AFM image of the emerging network of CNTs; d) μ-Raman spectra of MWCNTs obtained by λ=514 nm and λ=785 nm laser line excitations (green and red spectra, respectively).

3.3 Morphology Structure and properties of TiO_2/MWCNT/Stainless-Steel Metal Grating Composite

The morphology and the structure of the TIP impregnated MWCNTs/stainless steel, after calcination in air at 400°C, are SEM and TEM imaged in Fig. 3. From the low resolution top-view SEM images (Fig. 3a,b and the inset therein) an envelope of many aggregated particles can be highlighted, which identifies a highly compact network of carbon nanotubes.

Information about the structure at the nanoscale comes from the HRTEM image of the composite, where the interphase between a carbon nanotube and TiO_2 nanoparticles is shown in Fig. 3c. In particular, beside a MWCNT having about 40 walls, TiO_2 nanocrystals about 5-6 nm in size are observed, whose crystalline nature is testified by the presence of well-defined interference fringes 0.35 nm spaced, which correspond to the (101) anatase crystalline planes.

A different region, far from the TiO_2/MWCNTs interphase, is HRTEM imaged in Fig. 4a, together with the corresponding filtered image (Fig. 4b), where highly crystalline TiO_2 nanoparticles are evidenced. Moreover, from the unfiltered and filtered inverse fast-Fourier transforms (IFFTs) of the selected region (inserts respectively in Fig. 4a and 4b), the nanoparticle domains have been identified.

In fact, from the interference fringes on the filtered image (Figure 4b), obtained by selecting almost all the spots of filtered inverse fast-Fourier transform (IFFT) (insert in Fig. 4b), domains ranging in the 5-10 nm interval can be easily estimated.

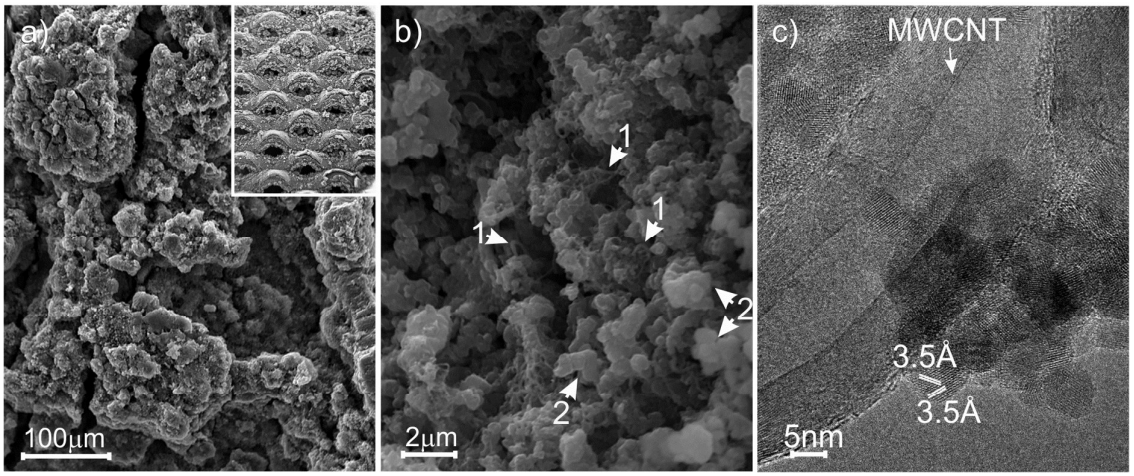

Fig. 3. a) Top-view SEM images of the TIP impregnated MWCNTs/stainless steel metal grating after the thermal treatment at 400°C; b) enlarged view of a selected area on (a) SEM image; c) HRTEM image of a CNT-TiO_2 junction region.

Table 1. Surface area and porosity properties.

	S_{BET} [a] (m^2/g)	S_{micro} [b] (m^2/g)	S_{meso} [b] (m^2/g)	% (S_{micro}) [c]	V_{Tot} [d] (cm^3/g)
TiO_2/MWCNT hybrid scaffold obtained from the composite grating@400°C	168	30	138	~18%	0.3946
TiO_2 @400°C	146	-	146	100%	0.1453

[a] Evaluated in the 0.1 < P/P_0< 0.3 pressure range; [b] Estimated using the *t-plot* method (*Harkins and Jura thickness curve*); [c] %(S_{micro}) = S_{micro}/S_{BET} x100; [d]Total pore volume (V_{Tot}) calculated as the volume of the liquid at P/P_0 » 0.975

Notice that mean sizes of about 6 nm have been obtained for TiO_2 nanoparticles, by means of the Scherrer's equation from XRD measurements. More details concerning the diffraction planes can be obtained from the HRTEM image (Fig. 4c) of a selected TiO_2 nanoparticle (dotted square in Fig. 4a).

Well-defined interference fringes, 0.35 nm and 0.19 nm spaced, corresponding respectively to the {101} and {200} anatase planes, are evidenced. From the FFT pattern (Fig. 4d) and from the corresponding simulated electron diffraction pattern (Fig. 4e) of the selected region, the anatase [0,1,0] zone-axis direction is obtained.

The optical properties of the TiO_2/MWCNTs/stainless-steel composite and of TiO_2 powders, obtained by the same sol–gel method for MWCNTs/TiO_2 composites, have been investigated by UV–vis spectroscopy in the reflectance mode (DR) and the results obtained in the 28000–23500 cm^{-1} interval are shown in Fig. 5. In the same figure the spectrum of the reference material (P25 TiO_2) is reported for the sake of comparison.

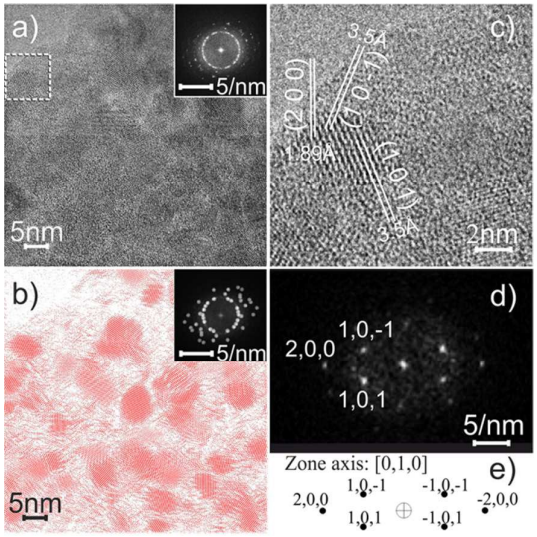

Fig. 4. a) HRTEM image of a region of TiO_2/MWCNTs/metal grating composite (insert: unfiltered inverse fast-Fourier transforms, IFFT); b) HRTEM filtered image of a) (insert: filtered inverse fast-Fourier transforms IFFT); c) HRTEM image of a selected region on a); d) experimental IFFT image oriented along the [010] zone axis; e) simulated SAED pattern, as obtained from the experimental IFFT image.

From this figure, it can be inferred that the absorption edges of the TiO_2/MWCNT/stainless steel composite (circles) and of the as prepared TiO_2 nanopowder (squares) are slightly red- and blue-shifted, respectively, with respect to that of P25 TiO_2 used as a reference material (dark triangles). The observed absorption edge of the as prepared TiO_2-based material is in agreement with the small dimensions (3-10 nm) of the anatase nanoparticles with respect to those of P25. Besides, the observed adsorption edge of P25 reflects the simultaneous presence of the anatase and rutile TiO_2 nanocrystals, 10-30 nm and ~15-30 nm in size, respectively. It is worth noticing that the more appreciable red shift observed for the TiO_2 hybrid composite material, which is mainly due to the ascertained presence of MWCNTs in the composite grating, may play a positive role in the adsorption of the visible light, to be used for photocatalysis or photodegradation applications.

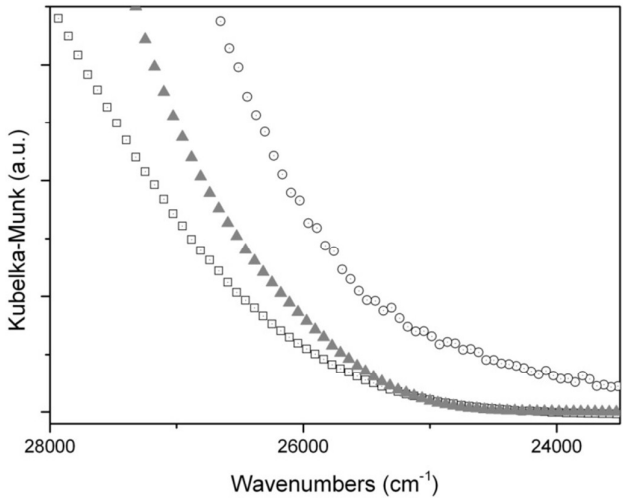

Fig. 5. UV-vis diffuse reflectance spectra of: TiO_2/MWCNTs/stainless steel (O); pure TiO_2powder obtained by the same sol–gel method for MWCNTs/TiO_2 composites (□), P25 TiO_2 (▲).

From the comparison of the volumetric N_2-adsorption/desorption isotherms of the TiO_2/MWCNT hybrid and of the pure TiO_2 material obtained by the same sol–gel method used for MWCNTs/TiO_2 composites (Fig. S2, ESI†), the BET surface area (S_{BET}), the micropore, mesopore and pore volume of the two samples are obtained, as reported in Table 1. From the shapes of the adsorption/desorption branches a mixed microporous/mesoporous

character is inferred for the TiO_2/MWCNT hybrid structure, while the pure TiO_2 is essentially mesoporous. Further differences can be highlighted from the shape and location of the hysteresis loops.

More in detail, the pure TiO_2 material is dominated by a mesopore contribution in the 40-90 Å range, while the pore size distribution of the TiO_2/MWCNTs hybrid structure is much more complex. In fact the TiO_2/MWCNTs hybrid structure shows a micropore family in the 8–20 Å range (presumably arising from MWCNTs) and a wide and complex distribution of mesopores ranging in 20-50 Å, 50-100 Å, 150-200 Å and >250 Å intervals. These results are in agreement with the pore size distribution (PSDs) obtained by the DFT model (Fig. S2b, ESI†) and by the Barrett-Joyner-Halenda (BJH) analysis (data not shown for the sake of brevity). It is worth noticing that the pores complex evolution of the TiO_2/MWCNTs hybrid nanostructures may play a role, which is higher than that of TiO_2 @ 400°C.

The porous character of the TiO_2-based materials looks ideal to test the photocatalytic degradation of methylene blue. Dimensions of MB along the main perpendicular directions (obtained as nucleus–nucleus distances) are reported in Fig. S3 (ESI†). Photodegradation experiments were performed by measuring in water solutions the decrement of the MB concentration adsorbed on the TiO_2/MWCNTs composite grating and on the samples containing the same quantity of photocatalysts (as prepared nanocrystalline TiO_2 and P25 TiO_2) upon light exposure for increasing time (Fig. 6).

The MB band evolution on the TiO_2/MWCNT/stainless-steel composite, as a function of the exposure time under visible light, is shown in Fig. 6a. From this figure, it is shown, that the intensity of the two main MB bands at 15100 cm^{-1} and at 16450 cm^{-1}, which are assigned to monomeric and aggregated species,[5, 60] decreases with the exposure time. Depending on the concentration, MB in solution may show a distinct tendency to form agglomerates, made by monomeric and polymeric species in thermodynamic equilibrium. Even though a detailed assignment of these bands is outside the scope of this work and can be found elsewhere,[61] the MB photodegradation performances of the TiO_2/MWCNT/stainless-steel composite is compared to the well-known P25 TiO_2 photocatalyst in Fig. 6b.

At this point, notice that the photodegradation of anatase nanoparticles grafted on the MWCNT scaffold is more effective than what observed for the TiO_2 nanoparticles coming from the same temperature treatment. According to the literature, the photocatalytic/photovoltaic enhanced performance of TiO_2 due to the presence of carbon nanotubes is still debated.[13, 62-64] One of the most recognized explanations is that the electron transport is accelerated by MWCNTs, which can accept electrons from photoexcited TiO_2. The resulting photoluminescence intensity has been found to be quenched.[65] The PL quenching efficiency, which has been demonstrated to be proportional to the fraction of nanotubes mixed with TiO_2 nanoparticles,[66] has been also verified for TiO_2/MWCNTs/steel composite with respect to the discrete TiO_2 nanoparticles, obtained at the same temperature (Fig. S4, ESI†).

The hybrid composite system and the reference TiO_2 nanopowder (P25) have been tested in a continuous photocatalytic test performed for several cycles (Fig. 6c). Although the hybrid photocatalyst shows an initial lower photodegradation activity in comparison with P25, its photoactivity is preserved. On the contrary

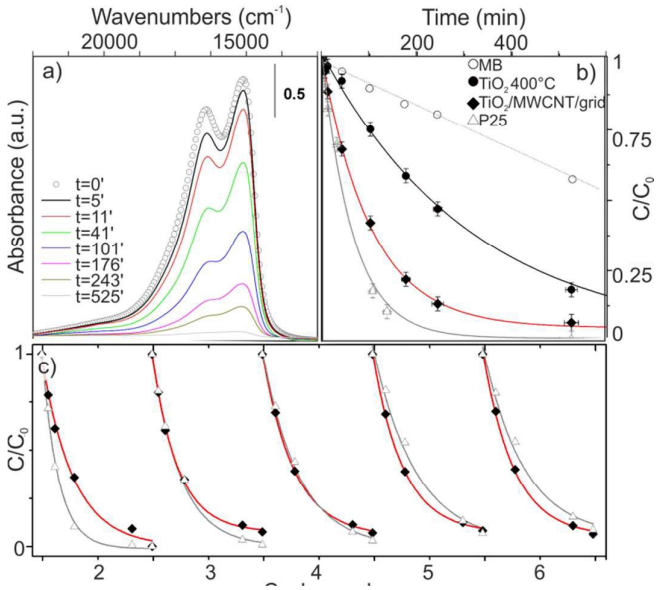

Fig. 6. a) Evolution of UV-visible spectra of MB (water solutions) adsorbed on TiO_2/MWCNT/stainless steel composite as a function of the exposure time under visible light (0, 5, 11, 41, 101, 176, 243 and 525 min); b) time dependence upon light exposure of pure MB surface concentration (C/C_0) (○), of MB adsorbed on TiO_2/MWCNTs/metal grating composite (◆) as compared to MB adsorbed on as-prepared TiO_2 (●) and on TiO_2 P25 reference material (△); c) performance in a cyclic photocatalytic test of the magnetically guided TiO_2/MWCNTs/metal system (◆) as compared to P25 nanopowder (△).

the P25 efficiency is progressively reduced, becoming lower than that of the hybrid material after the first number of cycles. Hence the photodegradation of the MB by a magnetically driven TiO_2/MWCNTs/steel composite has been shown very effective in the practical routine for its recyclability.

In conclusion, it comes that the MWCNTs forest can have a role: i) in reducing the recombination rate of the photogenerated electron-hole pairs due to the intimate contact between TiO_2 and MWCNTs, ii) in extending the frequency values in the visible range (CNTs act as a photosensitizer), iii) in acting as dispersing agent, iv) in inducing synergistic effects, v) in increasing the surface area of the material. Which of these factors is prevailing in our hybrid system goes beyond the scope of the present report. However, on the basis of our results a relevant role is played by the MWCNT in promoting the formation of a mesoporous scaffold.

Although the 304 austenitic stainless steel is expected to be only weakly ferromagnetic, notice that the obtained TiO_2/MWCNTs/stainless steel composite shows magnetic properties when a permanent magnet is approached (Fig. 7). The composite grating, placed in a glass becker containing a MB water solution, can be moved by an external magnet, while the dye photodegradation under solar light is occurring.

It is known that, upon thermal treatment of the austenic stainless steel, the iron remains in the form of austenite (fcc-phased Fe, γ-Fe) also stimulated by the presence of nickel, acting as a stabilizer. However, the magnetic properties of the austenitic stainless steel

can be modified by annealing/cooling steps, as well as by the growth of MWCNTs.[51] Carbon nanotubes can extract selectively iron (and not nickel) from the support to form α-Fe (bcc phase). α-Fe is magnetic and stable up to very high temperature (≈900°C). Moreover, by moving from MWCNTs to TiO_2/MWCNTs hybrid scaffolds, the surface properties change from hydrophobic to hydrophilic character (Fig. S5, ESI†). It comes that processes, like the water purification can take advantage from both the magnetic and the surface properties of the MWCNTs/stainless steel based composites. By following the literature, magnetically guided titania nanotubes have been proposed for site selective photocatalytic processes and drug release applications.[67]

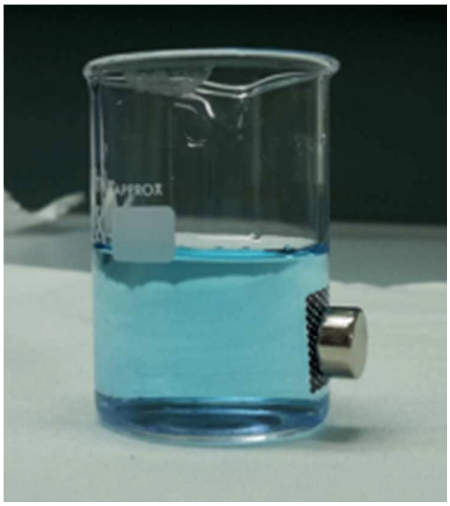

Fig. 7. A picture representing the multifunctional properties of the TiO_2/MWCNTs/steel composite.

4. Conclusions

In summary, a simple method for fabricating multifunctional nanostructured material, to be used for the efficient and convenient photodegradation of dyes in solutions, is reported. TiO_2/MWCNTs hybrid structures, grafted on a stainless steel support have been obtained by catalytic chemical vapour deposition of a dense forest of vertically oriented MWCNTs, followed by grafting of nanocristalline anatase TiO_2. Carbon nanotubes are entirely covering the stainless steel metal and form a porous scaffold, which acts as a templating phase for grafting TiO_2 nanoparticles, thus giving rise to a mesoporous TiO_2/MWCNTs hybrid texture. Notice that TiO_2 nanoparticles are well adhering to CNTs support.

According to the results, the enhanced photocatalytic efficiency of the composite for the MB degradation has been explained with the remarkable role played by MWCNTs, which act as pores former (medium-large mesopores), adsorbents, dispersing agents and electron reservoirs to trap electrons from the TiO_2 particles due to UV irradiation, and hence hindering the electron-hole pair recombination.

By taking into account the mechanical/thermal stability together with the magnetic properties of the steel support, moving from MWCNTs to TiO_2/MWCNTs hybrid scaffolds, the surface properties change from hydrophobic to hydrophilic in nature.

Moreover, the hybrid character of the nanostructured scaffold, well anchored to the withstanding support, together with its porosity and the magnetic nature of the entire composite, can make it suitable for a controllable processing of water photodegradation for environmental remediation.

Some more the optical and electrical properties of the TiO_2/MWCNTs hybrid system and of the MWCNTs porous scaffold/support may be taken under consideration to fabricate new functional structures, like sensors and energy materials.

Acknowledgements

This work was supported by MIUR (Ministero dell'Istruzione, dell'Università e della Ricerca), INSTM Consorzio, and NIS (Nanostructured Interfaces and Surfaces) Interdepartmental Centre of University of Torino.

Notes and references

1. I. Cobo, M. Li, B. S. Sumerlin and S. Perrier, *Nature Mater.*, 2015, **14**, 143-159.
2. O. Kozachuk, I. Luz, F. X. Llabrés I Xamena, H. Noei, M. Kauer, H. B. Albada, E. D. Bloch, B. Marler, Y. Wang, M. Muhler and R. A. Fischer, *Angew. Chem. Int. Ed.*, 2014, **53**, 7058-7062.
3. M. J. Uddin, D. E. Daramola, E. Velasquez, T. J. Dickens, J. Yan, E. Hammel and O. I. Okoli, *PSS-RRL*, 2014, **8**, 898-903.
4. S. Cravanzola, G. Haznedar, D. Scarano, A. Zecchina and F. Cesano, *Carbon*, 2013, **62**, 270–277.
5. S. Cravanzola, L. Muscuso, F. Cesano, G. Agostini, A. Damin, D. Scarano and A. Zecchina, *Langmuir*, 2015, **31**, 5469-5478.
6. M. M. Rahman, F. Bardelli, D. Scarano and A. Zecchina, *Catal. Today*, 2010, **150**, 84-90.
7. F. Cesano, D. Scarano, S. Bertarione, F. Bonino, A. Damin, S. Bordiga, C. Prestipino, C. Lamberti and A. Zecchina, 2008, **196**, 143-153.
8. G. Abellán, J. L. Jordá, P. Atienzar, M. Varela, M. Jaafar, J. Gómez-Herrero, F. Zamora, A. Ribera, H. García and E. Coronado, *Chem. Sci.*, 2015, **6**, 1949-1958.
9. T. Rodenas, I. Luz, G. Prieto, B. Seoane, H. Miro, A. Corma, F. Kapteijn, F. X. Llabrés i Xamena and J. Gascon, *Nature Mater.*, 2014, **14**, 48–55.
10. C. Cheng, A. Amini, C. Zhu, Z. Xu, H. Song and N. Wang, *Sci . Rep.*, 2014, **4**, 4181.
11. L. Yang, S. Luo, S. Liu and Q. Cai, *J. Phys. Chem. C*, 2008, **112**, 8939-8943.
12. Y. Yao, G. Li, S. Ciston, R. M. Lueptow and K. A. Gray, *Environ. Sci. Technol.*, 2008, **42**, 4952-4957.
13. K. Woan, G. Pyrgiotakis and W. Sigmund, *Adv. Mater.*, 2009, **21**, 2233-2239.
14. Z. Peining, A. S. Nair, Y. Shengyuan, P. Shengjie, N. K. Elumalai and S. Ramakrishna, *J. Photochem. Photobiol. A*, 2012, **231**, 9-18.

15. F. Alosfur, M. H. Haji Jumali, S. Radiman, N. J. Ridha, M. A. Yarmo and A. A. Umar, *Int. J. Electrochem. Sci.*, 2013, **8** 2977 - 2982.
16. F. Cesano, D. Pellerej, D. Scarano, G. Ricchiardi and A. Zecchina, *J. Photochem. Photob. a-Chem.*, 2012, **242**, 51-58.
17. J. Matos, J. Laine and J. M. Herrmann, *Appl. Catal. B: Environm.*, 1998, **18**, 281-291.
18. C. Y. Yen, Y. F. Lin, C. H. Hung, Y. H. Tseng, C. C. Ma, M. C. Chang and H. Shao, *Nanotechnology*, 2008, **19**, 045604.
19. G. Jiang, X. Zheng, Y. Wang, T. Li and X. Sun, *Powd. Technol-*, 2011, **207**, 465-469.
20. B. Gao, G. Z. Chen and G. Li Puma, *Appl. Catal. B*, 2009, **89**, 503-509.
21. S. Da Dalt, A. K. Alves and C. P. Bergmann, *Mater. Res. Bull.*, 2013, **48**, 1845-1850.
22. Y. Dong, D. Tang and C. Li, *Appl. Surf. Sci.*, 2014, **296**, 1-7.
23. J. Matos, A. García, L. Zhao and M. M. Titirici, *Appl. Catal. A Gen.*, 2010, **390**, 175-182.
24. D. G. Shchukin, J. H. Schattka, M. Antonietti and R. A. Caruso, *J. Phys. Chem. B*, 2003, **107**, 952-957.
25. N. Lakshminarasimhan, E. Bae and W. Choi, *J. Phys. Chem. C*, 2007, **111**, 15244-15250.
26. R. A. Caruso, A. Susha and F. Caruso, *Chem. Mater.*, 2001, **13**, 400-409.
27. F. Cesano, S. Bertarione, A. Damin, G. Agostini, S. Usseglio, J. G. Vitillo, C. Lamberti, G. Spoto, D. Scarano and A. Zecchina, *Adv. Mater.*, 2008, **20**, 3342.
28. F. Cesano, S. Bertarione, M. J. Uddin, G. Agostini, D. Scarano and A. Zecchina, *J. Phys. Chem. C*, 2011, **114**, 169-178.
29. Z. B. Lei, J. M. Li, Y. X. Ke, Y. G. Zhang, H. C. Zhang, F. Q. Li and J. Y. Xing, *J. Mater. Chem.*, 2001, **11**, 2930-2933.
30. A. S. Nair, Z. Peining, V. J. Babu, Y. Shengyuan and S. Ramakrishna, *PCCP*, 2011, **13**, 21248-21261.
31. D. G. Shchukin and R. A. Caruso, *Chem. Mater.*, 2004, **16**, 2287-2292.
32. J. Shi, C. Sun, M. B. Starr and X. Wang, *Nano Lett.*, 2011, **11**, 624-631.
33. F. Sordello, C. Duca, V. Maurino and C. Minero, *Chem. Comm.*, 2011, **47**, 6147-6149.
34. Y. D. Xia and R. Mokaya, *J. Mater. Chem.*, 2005, **15**, 3126-3131.
35. J. G. Yu, H. T. Guo, S. A. Davis and S. Mann, *Adv. Funct. Mater.*, 2006, **16**, 2035-2041.
36. F. Cesano, G. Agostini and D. Scarano, *Thin Solid Films*, 2015, **590**, 200-206.
37. C. Aprile, A. Corma and H. Garcia, *PCCP*, 2008, **10**, 769-783.
38. J. N. Kondo, T. Yamashita, K. Nakajima, D. Lu, M. Hara and K. Domen, *J. Mater. Chem.*, 2005, **15**, 2035-2040.
39. J. H. Pan, Z. Lei, W. I. Lee, Z. Xiong, Q. Wang and X. S. Zhao, *Catal. Sci. Technol.*, 2012, **2**, 147-155.
40. E. Ortel, S. Sokolov and R. Kraehnert, *Micropor. Mesopor. Mat.*, 2010, **127**, 17-24.
41. J. Shang, W. Li and Y. Zhu, *J. Moi. Catal. A*, 2003, **202**, 187-195.
42. S. Sokolov, E. Ortel and R. Kraehnert, *Mater. Res. Bull.*, 2009, **44**, 2222-2227.
43. S. Sokolov, E. Ortel, J. Radnik and R. Kraehnert, *Thin Solid Films*, 2009, **518**, 27-35.
44. M. A. Anderson, A. L. Cudero and J. Palma, *Electrochim. Acta*, 2010, **55**, 3845-3856.
45. L. Camilli, M. Scarselli, S. Del Gobbo, P. Castrucci, F. Nanni, E. Gautron, S. Lefrant and M. De Crescenzi, *Carbon*, 2011, **49**, 3307-3315.
46. Y. Chen, Z. Lv, J. Xu, D. Peng, Y. Liu, J. Chen, X. Sun, C. Feng and C. Wei, *J. Power Sources*, 2012, **201**, 136-141.
47. S. Minnikanti, P. Skeath and N. Peixoto, *Carbon*, 2009, **47**, 884-893.
48. J. J. Moore, J. H. Kang and J. Z. Wen, *Mater. Chem. Phys.*, 2012, **134**, 68-73.
49. N. Sano, Y. Hori, S. Yamamoto and H. Tamon, *Carbon*, 2012, **50**, 115-122.
50. L. Camilli, P. Castrucci, M. Scarselli, E. Gautron, S. Lefrant and M. De Crescenzi, *J. Nanopart. Res.*, 2013, **15**, 1846.
51. L. Camilli, M. Scarselli, S. Del Gobbo, P. Castrucci, F. R. Lamastra, F. Nanni, E. Gautron, S. Lefrant, F. D'Orazio, F. Lucari and M. De Crescenzi, *Carbon*, 2012, **50**, 718-721.
52. C. T. Wirth, B. C. Bayer, A. D. Gamalski, S. Esconjauregui, R. S. Weatherup, C. Ducati, C. Baehtz, J. Robertson and S. Hofmann, *Chem. Mater.*, 2012, **24**, 4633-4640.
53. F. Cesano, I. Rattalino, F. Bardelli, A. Sanginario, A. Gianturco, A. Veca, C. Viazzi, P. Castelli, D. Scarano and A. Zecchina, *Carbon*, 2013, **61**, 63-71.
54. R. P. Vidano, D. B. Fischbach, L. J. Willis and T. M. Loehr, *Solid State Commun.*, 1981, **39**, 341-344.
55. G. Cravotto, D. Garella, E. Calcio Gaudino, F. Turci, S. Bertarione and G. Agostini, *New J. Chem.*, 2011, **35**, 915-919.
56. J. H. Lehman, M. Terrones, E. Mansfield, K. E. Hurst and V. Meunier, *Carbon*, 2011, **49**, 2581-2602.
57. M. S. Shamsudin and S. M. Sanip, *Adv. Mater. Res.*, 2015, **1109**, 509-513.
58. E. F. Antunes, A. O. Lobo, E. J. Corat, V. J. Trava-Airoldi, A. A. Martin and C. Veríssimo, *Carbon*, 2006, **44**, 2202-2211.
59. W. Li, H. Zhang, C. Wang, Y. Zhang, L. Xu, K. Zhu and S. Xie, *Appl. Phys. Lett.*, 1997, **70**, 2684-2686.
60. F. Cesano, M. M. Rahman, S. Bertarione, J. G. Vitillo, D. Scarano and A. Zecchina, *Carbon*, 2012, **50**, 2047-2051.
61. M. J. Uddin, F. Cesano, F. Bonino, S. Bordiga, G. Spoto, D. Scarano and A. Zecchina, *J. Photochem. Photob. A Chem.*, 2007, **189**, 286-294.
62. B. Gao, G. Z. Chen and G. Li Puma, *Appl. Catal. B Environ.*, 2009, **89**, 503-509.
63. B. Gao, C. Peng, G. Z. Chen and G. Li Puma, *Appl. Catal. B Environ.*, 2008, **85**, 17-23.
64. Y. Yu, J. C. Yu, J. G. Yu, Y. C. Kwok, Y. K. Che, J. C. Zhao, L. Ding, W. K. Ge and P. K. Wong, *Appl. Catal. A Gen.*, 2005, **289**, 186-196.
65. D. Y. Lee, C. Y. Shin, S. J. Yoon, H. Y. Lee, W. Lee, N. K. Shrestha, J. K. Lee and S. H. Han, *Sci. Rep.*, 2014, **4**, 3930 (3931-3935).
66. A. Stevanovic, S. Ma and J. T. Yates, *J. Phys. Chem. C*, 2014, **118**, 23614-23620.

67. N. K. Shrestha, J. M. Macak, F. Schmidt-Stein, R. Hahn, C. T. Mierke , B. Fabry and P. Schmuki, *Angew. Chem.*, 2009, **121**, 987 -990.